PCCP

PAPER

View Article Online
View Journal | View Issue

Cite this: *Phys. Chem. Chem. Phys.*, 2026, **28**, 8136

Sources of non-Arrhenius electron transport in bacterial nanowires

Kiriko Terai, †[a] Peng Zhang[a] and David N. Beratan *[abc]

Received 22nd December 2025,
Accepted 2nd March 2026

DOI: 10.1039/d5cp04984a

rsc.li/pccp

Electron transport in biological redox chains typically follows an Arrhenius law, with rates and conductivities that increase with temperature. Surprisingly, bacterial nanowires show anti-Arrhenius transport. We simulated electron transport in a one-dimensional OmcS nanowire model from 275 K to 375 K using continuum electrostatic analysis of structural snapshots drawn from classical molecular dynamics simulations. We found that the electron-transport rate increases with temperature from 300–375 K, but more slowly than an Arrhenius law predicts. This softened temperature dependence is attributed primarily to temperature-dependence of the reaction free energies. Protein electrostatic interactions contribute to the weakened temperature dependence, but the effects are not large enough to invert the temperature dependence. The origins of anti-Arrhenius conduction is likely rooted in structural and dynamical factors beyond our model, including configuration-specific solvent interactions and entropy effects missing from the implicit-solvent treatment, as well as multidimensional transport pathways that may arise in bundled, cross-linked, or biofilm-embedded nanowire networks.

1 Introduction

The exponential growth of reaction rates with temperature is described by the classical Arrhenius rate law, and this Arrhenius behavior is often observed for biological charge transport chains that operate near room temperature. In contrast, anti-Arrhenius behavior is typically associated with electron transport that is fast compared to carrier trapping time scales.[1,2] Yet, some soft matter systems exhibit anti-Arrhenius electron transport, including bacterial nanowires,[3] cobalt-based metal organic frameworks,[4] conjugated polymer systems,[5–7] and quantum dot assemblies.[8] Finding anti-Arrhenius transport challenges the theoretical understanding of electron transport in bacterial nanowires, usually described in terms of Marcus-like multi-step electron hopping between localized states, with nuclear tunneling corrections at lower temperatures.[9,10] As such,the physical origins of anti-Arrhenius transport in bacterial nanowires is poorly understood. Some have suggested that the observed temperature dependence points to a metallic-like transport mechanism.[11]

Some anaerobic bacteria, including *Geobacter sulfurreducens* and *Shewanella oneidensis*, use extracellular electron transport *via* nanowires to deliver electrons to extracellular electron acceptors. Nanowires are of interest for applications in emerging bioinspired and biohybrid technologies, including microbial fuel cells, microbial electrosynthesis, and bioelectronics.[12,13] Bacterial nanowires also enable the exchange of electrons among bacterial cells.[14,15] Electron transport through nanowires can occur on micrometer length scales,[16] and nanowires can be as conductive as some conducting organic polymers.[14] Nanowire conductivity is believed to arise from heme-rich, cytochrome-based assemblies. *Geobacter* nanowires are filamentous protein appendages that contain multiheme cytochromes, including OmcS, OmcZ, and OmcE.[17–20] *Shewanella* nanowires are filamentous outer-membrane and periplasmic extensions that contain multiheme cytochromes, including OmcA, STC, MtrABC, and MtrDEF.[15,21–28] The physiologically relevant temperature range for bacterial nanowires is about 280–300 K,[12] and the proteins are stable at higher temperatures. Nanowires begin to denature above 350 K, but most of the constituent proteins retain their structure up to 375 K.[29,30]

Thermally activated multi-step hopping transport (between spatially localized states) is the most familiar mechanism for biological electron transport because heme–heme interactions are so weak.[9,31–37] As such, electron-transfer rates through bacterial nanowires are expected to increase as the temperature grows, since hopping is thermally activated, with an activation free energy predicted by Marcus-like theories.[10] Yet, experiments find that the conductivities of *Geobacter* OmcS nanowires decrease by about 10% from 275 to 340 K,[38,39] behavior that is not consistent with thermally activated hopping.[40]

[a] *Department of Chemistry, Duke University, Durham, NC 27708, USA. E-mail: david.beratan@duke.edu*
[b] *Department of Physics, Duke University, Durham, NC 27708, USA*
[c] *Department of Biochemistry, Duke University, Durham, NC 27710, USA*
† Current address: Department of Chemistry, University of North Carolina at Chapel Hill, Chapel Hill, NC 27599, USA.

A drop in conductivity with increasing temperature is found in metals, where electron–phonon scattering increases with temperature.[41,42] The detailed nature of charge transport through bacterial nanowires remains poorly understood. Early studies suggested many possible mechanisms, including incoherent multi-step hopping,[43,44] coherent transport,[3,45] or incoherent transport between delocalized islands.[46–48] While much structural evidence supports a thermally activated mechanism,[43,49–51] the decrease in conductivity with temperature is not entirely consistent with a thermally activated hopping mechanism.[38,39,52] The aim of this study is to understand how changes in temperature may influence nanowire transport. In particular, we study how the multi-step hopping parameters may, themselves, change as a function of temperature in *Geobacter* OmcS nanowires.

Earlier theoretical studies of anti-Arrhenius transport in OmcS nanowires examined transport at two temperatures within a narrow range.[52,53] These studies do not address the more general temperature dependence for transport in these structures. Here, we examine transport across a wider temperature range. Dahl *et al.* suggested that electron-transfer rates in the OmcS nanowire increase with cooling from 310 K to 270 K because of hydrogen bonding network reconstructions.[52] Quantum mechanics/molecular mechanics studies of Guberman-Pfeffer (at 270 K and 300 K) found that incoherent hopping models fail to explain measured conductivities in those studies.[52,53] Our modeling explores how the conductivity of *Geobacter* OmcS nanowires change with temperature from 275 to 375 K, exploring how temperature dependent protein structural changes may influence electron-transfer rates and conductivities[54] through changes in the key electron hopping parameters: electronic couplings, reorganization energies, and reaction free energies.

2 Modeling transport in nanowires

Cryo-EM data find that individual nanowires (*i.e.*, nanowire fibers) are filamentous assemblies of multi-heme cytochromes with hemes that align to form a one-dimensional hopping chain (Fig. 1).[15,18,51,55,56] OmcS nanowire fibers contain hundreds of hexa-heme cytochrome OmcS protein monomers. Each monomer is about 4.8 nm in length, and the hemes are oriented along the fiber axis. Each heme in OmcS has two nearest-neighbor hemes, and neighboring heme pairs have parallel or T-shaped orientations. The protein wraps around the central heme chain. The diameter of the fiber is ~4 nm, and the hemes have limited solvent exposure. The hemes of OmcS are redox active, and heme-to-heme hopping is believed to mediate the transport.[51] We begin by modeling the OmcS fiber structure and computing temperature dependent electron-transfer parameters for nearest-neighbor hopping between hemes. We assume only nearest-neighbor hopping, because the next-nearest-neighbor electronic couplings are expected to be very weak, leading to electron transfer rates that are negligible on the timescales considered here.

MD simulations were performed on a heptamer of the OmcS hexa-heme protein, based on a cryo-EM structure of Wang *et al.* (PDB ID: 6EF8[18]). We used the Amber24 program package[57,58]

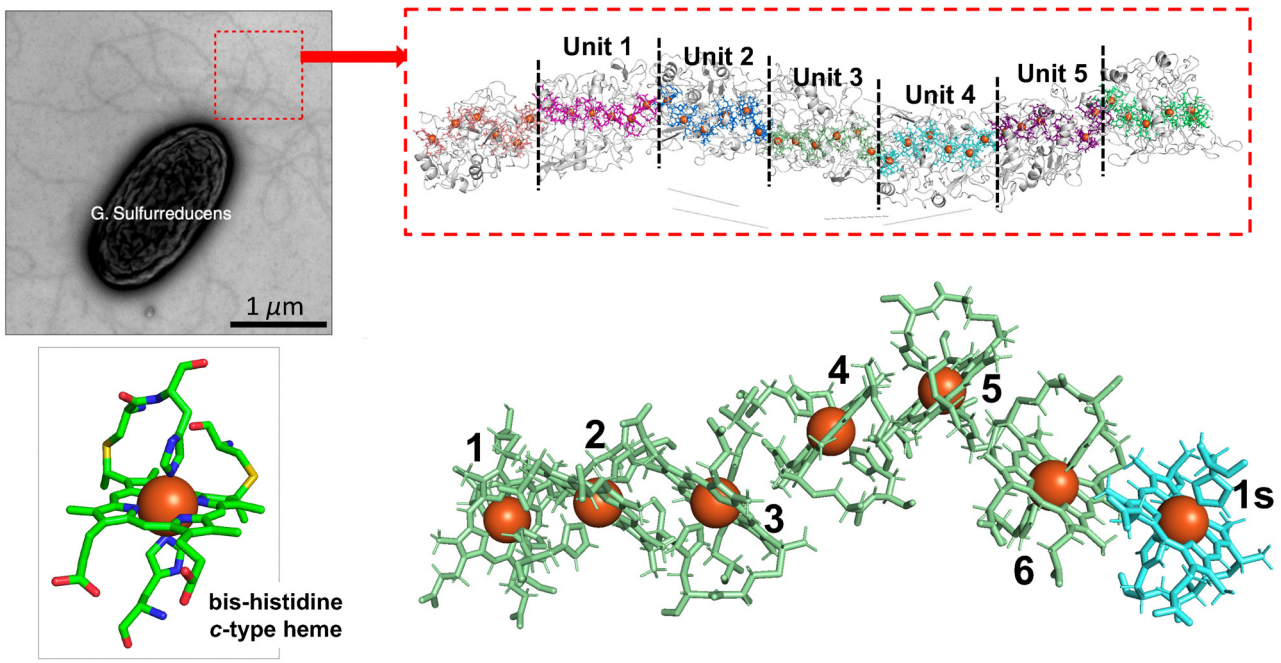

Fig. 1 Model of a hexa-heme OmcS protein nanowire of *Geobacter sulfurreducens* as a one-dimensional hopping chain based on the cryo-EM structure of OmcS.[18] A transmission electron microscope image of *G. sulfurreducens* is shown (reproduced from ref. 17), and the crystal structure of a heptamer assembly of the OmcS hexa-heme protein (PDB ID: 6EF8[18]) that was used in our MD simulations. Each monomer unit with six bis-histidine c-type hemes is labeled unit 1, unit 2, unit 3, unit 4, and unit 5, excluding the terminal monomers. Hemes within each unit are numbered 1 to 6, and 1s denotes the first heme of the adjacent unit. The rate constant for electron transfer from the n-th to the $(n + 1)$-th heme is $k_{n\to n+1}$.

with the ff19SB force field to describe the protein backbone and side chains,[59] the OPC water model,[60] and a force field that was parameterized to describe bis-histidine coordinated c-type hemes (Fig. 1).[61] A heptamer of the OmcS protein complex with surrounding water molecules was used at the start of the MD simulation in a 100 × 99 × 373 Å^3 box, and 105 Na^+ ions were added to establish system neutrality. The solvated protein heptamer was gradually heated from 100 K to the target temperature over 1 ns with constant volume conditions (NVT equilibration). We then carried out a series of NPT equilibration runs in which harmonic positional restraints on the protein heavy atoms were progressively relaxed. Specifically, we performed five consecutive 1 ns NPT equilibrations with restraint force constants of 100, 10, 1, 0.1, and 0 kcal mol^{-1} Å^{-2}, respectively, thereby releasing the restraints stepwise until the protein was fully unrestrained. After equilibration, MD production simulations were conducted for 75 ns at 275, 300, 325 K, and 350 K, and for 150 ns at 375 K. Structural snapshots were collected for the 50–75 ns window for 275–350 K simulations, and for the 125–150 ns window for the 375 K simulations. These snapshots were used to compute the temperature-dependent electron-transfer parameters, as described below. During these production runs, the protein backbone RMSD is ~2 Å at 275–325 K, ~2–3 Å at 350 K, and ~2–4 Å at 375 K (see SI), consistent with increased thermal flexibility at high temperatures without evidence of large-scale unfolding. The overall protein fold is likely preserved across the full temperature range studied.

2.1 Heme-to-heme electron hopping rates

Protein electron transport often occurs *via* (incoherent) multi-step hopping between cofactors.[35,36] The cofactor-to-cofactor couplings in OmcS are too small and the energy disorder is too large to support coherent delocalization or even "flickering resonance" transport.[31,32,35,62] Transport seems more likely to occur by non-adiabatic multi-step hopping. The electron transfer rate from heme i to heme j ($k_{i\to j}$) is approximated by the non-adiabatic Marcus-like rate expression:[9,10,63]

$$k_{i\to j} = \frac{2\pi}{\hbar}\langle V_{ij}^2\rangle \frac{1}{\sqrt{4\pi\lambda_{ij}k_B T}} \exp\left[-\frac{\left(\Delta G_{ij}^{(0)} + \lambda_{ij}\right)^2}{4\lambda_{ij}k_B T}\right] \quad (1)$$

where $\langle V_{ij}^2\rangle$ is the mean-squared electronic coupling between hemes i and j, λ_{ij} is the corresponding reorganization energy, and $\Delta G_{ij}^{(0)}$ is the standard reaction free energy. If these three parameters are temperature independent, the hopping rates will grow with temperature, consistent with the Marcus and Arrhenius theories.

At edge-to-edge distances longer than 3 Å, electron hopping is expected to be sufficiently slow that the Marcus-like (quasi-equilibrium) non-adiabatic electron transfer theory framework is expected to be valid, and we base our assessment of the electron transfer parameters on conformational averaging derived from MD sampling. For each MD snapshot, we calculate the electronic coupling, reorganization energy, and reaction free energy for every nearest-neighbor heme pair. These quantities are first obtained on a per-snapshot basis. For each heme pair at a given temperature, we then ensemble-average the electronic couplings, reorganization energies, and reaction free energies over all snapshots, and use these averaged values in eqn (1) to determine the electron transfer rate constants between nearest-neighbor hemes. MD snapshots are extracted every 10 ps, so fluctuations on this time scale and longer are captured. We repeated the MD simulations at 275, 300, 325, 350, and 375 K to explore the effects of temperature on transport.

2.2 Reorganization energies

The reorganization energy (λ) for electron transfer is the free energy required to shift the nuclear configuration from the geometry of its equilibrium initial state (D^-A) to the geometry of its final equilibrium state (DA^-) without transferring an electron.[10,64] This energy has inner- and outer-sphere contributions.[10,64,65] We computed the outer-sphere contributions to λ, which are larger than the inner sphere contribution for most heme proteins.[53,65,66]

The reorganization energies were computed using a finite difference Poisson–Boltzmann (FDPB) method[64] implemented in the DelPhi software package,[67–70] as in prior studies.[71–73] The reorganization energies were calculated using eqn (2)[64]

$$\lambda = \frac{1}{2}\sum_i \left(\delta\phi_i^{d^*d} - \delta\phi_i^{ad}\right) dq_i^{ad}, \quad (2)$$

where dq_i^{ad} is the change in charge on atom i upon electron transfer, $\delta\phi_i^{d*d}$ is the potential change at atom i due to re-equilibration of the electronic polarization upon electron transfer, and $\delta\phi_i^{ad}$ is the potential change at atom i that arises from re-equilibration of the electronic polarization and nuclear reorientation. The restrained electrostatic potential (RESP) charges[74] on the donor and acceptor (both bis-histidine c-type hemes) were calculated using Gaussian 16[75] at the density functional theory (DFT) level with the B3LYP functional.[76,77] The Def2SVP basis set[78] was used for C, H, O, N, and S atoms, and the ECP10MDF effective core potential[79] was used for iron. This analysis produced dq_i^{ad} values for eqn (2).[72] The linearized PB equation (eqn (3)) with Debye–Hückel potential boundary conditions was solved to obtain $\delta\phi_i^x$ ($x = d^*d$ or ad) of eqn (2):[64]

$$\nabla\cdot\varepsilon\nabla\delta\phi^x = -4\pi\delta\rho^{ad} - 8\pi e^2 I\delta\phi^x/k_B T \quad (3)$$

where $\delta\rho^{ad}$ is the change in the atomic charge density upon electron transfer, and ε is the dielectric constant.

We modeled the system using three dielectric zones, corresponding to the protein, regions inside the protein where water molecules can reside, and bulk water surrounding the protein (Fig. 2), with dielectric constants ε_p, ε_c, and ε_w, respectively. To compute the reorganization energy using eqn (2), two calculations were performed, producing $\delta\phi_i^{d*d}$ and $\delta\phi_i^{ad}$.

To compute $\delta\phi_i^{ad}$, we used $\varepsilon_p = 4$. The values of ε_w were set to 87.15, 77.70, 69.29, 61.81, and 55.16 at 275, 300, 325, 350, and 375 K, respectively.[80] ε_c was set to 20, based on static dielectric constant estimates for water nanocavities.[81] The SI describes how

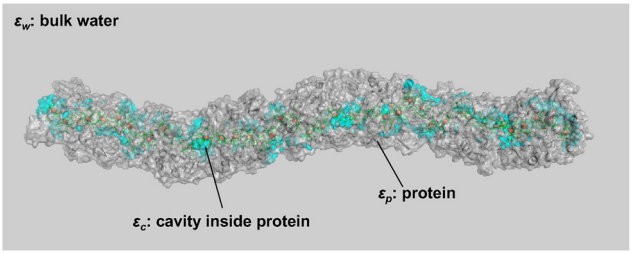

Fig. 2 The solvation model is shown for the OmcS heptamer structure, modeled with three dielectric zones: protein dielectric constant ε_p, internal cavity dielectric constant ε_c, and bulk solvent water dielectric constant ε_w.

the values of ε_c were estimated, and we find that the computation results of the reorganization energies are robust with respect to the chosen values. The ionic strength was set to 0.15 M.[64,72]

To compute $\delta\phi_i^{d*d}$, we used $\varepsilon_p = 2$ and $\varepsilon_w = 1.8$.[64,72,73] ε_c was set to 1.9, a value between the optical dielectric constants of protein and water. The ionic strength was set to zero.[64,72,73] We used a $601 \times 601 \times 601$ grid with a spacing of 2.0 grid points per Å; the convergence threshold total residual error in the potential was $1 \times 10^{-4} k_B T/e$.

2.3 Heme–heme couplings

The temperature dependent electronic couplings between nearest-neighbor hemes were approximated using a 1D square-barrier tunneling model[9] with parameters based on electronic structure calculations:

$$V_{ij}(r_{ij}) = V_0 \exp[-\beta(r_{ij} - r_0)/2] \quad (4)$$

The parameters $V_0 = 7.23$ meV, $\beta = 2.77$ Å^{-1}, $r_0 = 3.6$ Å were obtained from electronic structure analysis for stacked heme pairs, and $V_0 = 1.81$ meV, $\beta = 0.1$ Å^{-1}, $r_0 = 3.6$ Å were obtained for T-shaped heme pairs by fitting the computed electronic coupling values of Jiang *et al.*[82] The edge-to-edge distances between hemes, r_{ij}, were obtained from the MD snapshots at each temperature. The edge-to-edge distance is defined as the shortest distance between heavy atoms of the heme pairs, including the propionate side chains.[82] The mean squared electronic coupling was calculated by snapshot averaging the squared couplings.

2.4 Reaction free energies

We calculated the temperature dependent free energies for electron transfer from heme i to j using:

$$\Delta G_{ij}^{T=x} = \Delta G_{ij}^{T=300} + \Delta G_{ij}^{T=x,\mathrm{el}} - \Delta G_{ij}^{T=300,\mathrm{el}}. \quad (5)$$

$\Delta G_{ij}^{T=x}$ is the free energy for electron transfer from heme i to j at temperature x K. The superscript "el" denotes the electrostatic component of the free energy, the term $\frac{1}{2}\sum_i \delta\phi_i^{ad} \mathrm{d}q_i^{ad}$ of eqn (2). The values $\Delta G_{ij}^{T=300}$ are taken from the study by Jiang *et al.*,[82] which reported reaction free energies that include both electrostatic and non-electrostatic contributions. We used the $\Delta G_{ij}^{T=300}$ values of ref. 82 as reference free energies at 300 K and computed the changes in the electrostatic contributions to the free energy with temperature, using the assumption that temperature-dependent changes to the reaction free energy are dominated by electrostatic fluctuations. Other contributions (such as those arising from heme distortions,[83,84] heme–heme interactions,[85–87] and hydrogen bond network changes[88,89]) are not captured by our model. The assumption that electrostatic fluctuations dominate the temperature dependence of reaction free energies is supported by the findings of ref. 53, which showed that electrostatic interactions among the hemes, protein, and solvent predominantly determine the temperature dependence of heme redox potentials.

2.5 Mean first passage time and effective electron transport rates

After computing the temperature dependent electron-transfer parameters that appear in eqn (1), we calculated the mean first passage time[90,91] for transport between heme 1 of unit 1 and heme 6 of unit 5 (see Fig. 1). Each repeating unit in our model contains 6 hemes, so the full system in the mean first passage time analysis includes 30 hemes.

The rate matrix for electron transfer among the hemes in units 1 through 5 of the OmcS heptamer is denoted by K (eqn (6)). We assume that electron transfer occurs between nearest-neighbor hemes, and all rates between non-nearest neighbors are set to zero. The matrix element K_{ji} is the electron transfer rate constant from the i-th to the j-th heme ($i, j = 1, 2, \ldots, 30$), and the diagonal elements K_{ii} are defined as the negative sum of all elements in the i-th column. We treat the final heme (the 30th heme in repeating unit 5) as an irreversible trap. Specifically, the forward rate from the 29th to the 30th heme, $K_{30,29}$, is nonzero, whereas the reverse rate, $K_{29,30}$, is set to zero.

$$\mathbf{K} = \begin{bmatrix} -k_{1\to2} & k_{2\to1} & \cdots & 0 \\ k_{1\to2} & -(k_{2\to1}+k_{2\to3}) & \cdots & \vdots \\ 0 & k_{2\to3} & \cdots & \vdots \\ \vdots & \vdots & \ddots & \vdots \\ \vdots & \vdots & k_{29\to28} & 0 \\ \vdots & \vdots & -(k_{29\to28}+k_{29\to30}) & 0 \\ 0 & 0 & 0 & 0 \end{bmatrix} \quad (6)$$

To compute the mean first passage time for electron transport from unit 1 to unit 5 in the OmcS heptamer, we work with a reduced rate matrix $\tilde{\mathbf{K}}$ that only includes the non-trap states (eqn (7)).[90,91] The matrix $\tilde{\mathbf{K}}$ is obtained by removing the row and column corresponding to the trap site from K (eqn (6)).[90,91]

$$\tilde{\mathbf{K}} = \begin{bmatrix} -k_{1\to2} & k_{2\to1} & \cdots & 0 \\ k_{1\to2} & -(k_{2\to1}+k_{2\to3}) & \cdots & \vdots \\ 0 & k_{2\to3} & \cdots & \vdots \\ \vdots & \vdots & \ddots & 0 \\ \vdots & \vdots & \cdots & k_{29\to28} \\ 0 & 0 & \cdots & -(k_{29\to28}+k_{29\to30}) \end{bmatrix} \quad (7)$$

The reduced rate matrix describes the dynamics of the system while it remains in the non-trap subspace.[90,91] The

probability to leave this subspace *via* a transition from the 29th heme to the trap, encoded in the diagonal element $\tilde{K}_{29,29}$, is interpreted as arrival at the 30th heme.

The mean first passage time is calculated using:[90]

$$\langle \tau \rangle = \sum_i \left[-\tilde{\mathbf{K}}^{-1} \tilde{\mathbf{p}}_0 \right]_i \quad (8)$$

where $\tilde{\mathbf{p}}_0$ is the initial population vector for all sites except the trap. Here, we take the electron to be initially localized on the first heme, so $\tilde{\mathbf{p}}_0 = (1, 0, 0, \ldots)^T$.

Since the conductivity describes how quickly the electrons transit the chain,[54] we approximate the effective electron transport rate across the OmcS heptamer as the inverse of the mean first passage time:

$$k_{\text{eff}} = \frac{1}{\langle \tau \rangle}. \quad (9)$$

3 Results and discussion

3.1 Computed electron transfer parameters

The calculated temperature dependent reorganization energies, reaction free energies, mean-square electronic couplings, and the resulting electron transfer rate constants for nearest-neighbor heme-to-heme electron transfer in monomer unit 3 of the OmcS heptamer (Fig. 1) are shown in Fig. 3A–D, respectively. Results for units 1, 2, 4, and 5 are provided in the SI. Similar qualitative and quantitative trends in the key electron transfer parameters are found in all monomer units of the OmcS heptamer. As such, we focus here on the computed results for unit 3. The SI compares our computed reorganization energies, reaction free energies, and mean-square electronic couplings at 275 K and 300 K with those reported in ref. 52, 53 and 82.

The electron-transfer parameters depend nonlinearly and non-monotonically on temperature, and the temperature dependence of these parameters are very weak. Over the examined temperature range, the reorganization energies vary within only $\sim$0.01 eV, the reaction free energies within $\sim$0.005 eV, and the mean-square electronic couplings within $\sim 3 \times 10^{-5}$ eV^2, with no systematic increase or decrease. No significant changes were observed in the edge-to-edge distances between the heme pairs (see SI). Since the temperature-dependence of the parameters is so weak, the electron transfer rate constants between nearest-neighbor heme pairs are predicted to increase with temperature, in a manner that is qualitatively consistent with the Arrhenius rate law. Next, we study how these small temperature-dependent changes in the electron-transfer parameters may influence the effective electron transport rate's temperature dependence.

3.2 Computed effective electron transport rates

The calculated effective electron transport rates to traverse monomer units 1 through 5 of the OmcS heptamer (eqn (9)) are shown in Fig. 4. The effective electron transport rate was computed in five ways: (1) by including temperature dependence in all of the electron-transfer parameters (scheme a), (2) by assuming that all electron-transfer parameters are temperature independent (scheme b), (3) by including the temperature dependence of only the mean squared electronic couplings (scheme c), (4) by including the temperature dependence of only the reaction free energies (scheme d), and (5) by including the temperature dependence of only the reorganization energies (scheme e). The purpose of computing the effective electron transport rate using schemes b, c, d, and e is to identify sources of temperature dependent transport in the OmcS nanowires. We fit the effective electron transport rate using $\log\left(\frac{k_{\text{eff}}}{k_{\text{ref}}}\right)$ *vs.* $1/T$ where k_{eff} is the effective electron transport rate and $k_{\text{ref}} = 1\ \text{s}^{-1}$ is the reference rate, so that the argument of the logarithm is dimensionless. Going forward, we denote $\frac{k_{\text{eff}}}{k_{\text{ref}}}$ as k. With this convention, the slope give the Arrhenius parameter $-\frac{E_a}{k_B}$ (with units of K), where E_a is the activation energy of the effective electron transport through five monomer units of the OmcS heptamer and k_B is Boltzmann's constant.

Fig. 4A compares the effective electron transport rates computed with all electron transfer parameters treated as temperature-dependent (scheme a) or temperature-independent (scheme b). In scheme a, the effective electron transport rate increases by approximately 9.4-fold (275–300 K), 2-fold (300–325 K), 1.6-fold (325–350 K), and 1.4-fold (350–375 K), indicating a general increase in the effective electron transport rate with temperature. The corresponding slopes, obtained from linear fits of $\log(k)$ *vs.* $1/T$, are -1.225, -1.057, -1.036, and -1.026 K for each respective temperature interval. In scheme b, where temperature-independent electron transfer parameters produce Arrhenius behavior, the corresponding slopes, obtained from linear fits of $\log(k)$ *vs.* $1/T$ are -1.079 (275–300 K), -1.061 (300–325 K), -1.049 (325–350 K), and -1.040 (350–375 K).

In the 300–375 K range, the rate is predicted to increase with temperature in scheme a, but the rate speed up is weaker than the Arrhenius prediction. That is, the slope of the $\log(k)$ *vs.* $1/T$ plot in scheme a is softer than the slope in scheme b. In the 275–300 K range, the rate acceleration is more rapid than the Arrhenius prediction. That is, a steeper slope of the $\log(k)$ *vs.* $1/T$ plot is found in scheme a compared to that in scheme b. To identify the origin of these deviations from Arrhenius behavior, we next determine which temperature-dependent electron transfer parameters produce the differences in the computed effective electron transport rates.

Fig. 4B compares the effective electron transport rates computed for different sets of assumptions: all electron transfer parameters are temperature-dependent (scheme a), only the mean-square electronic coupling is temperature-dependent (scheme c), only the reaction free energy is temperature-dependent (scheme d), and only the reorganization energy is temperature-dependent (scheme e). In scheme c, the rate increases by approximately 2.3-fold (275–300 K), 2.2-fold (300–325 K), 1.8-fold (325–350 K), and 1.5-fold (350–375 K). In scheme d, the rate increases by approximately 10.8-fold (275–300 K), 1.9-fold (300–325 K), 1.7-fold (325–350 K), and 1.6-fold (350–375 K).

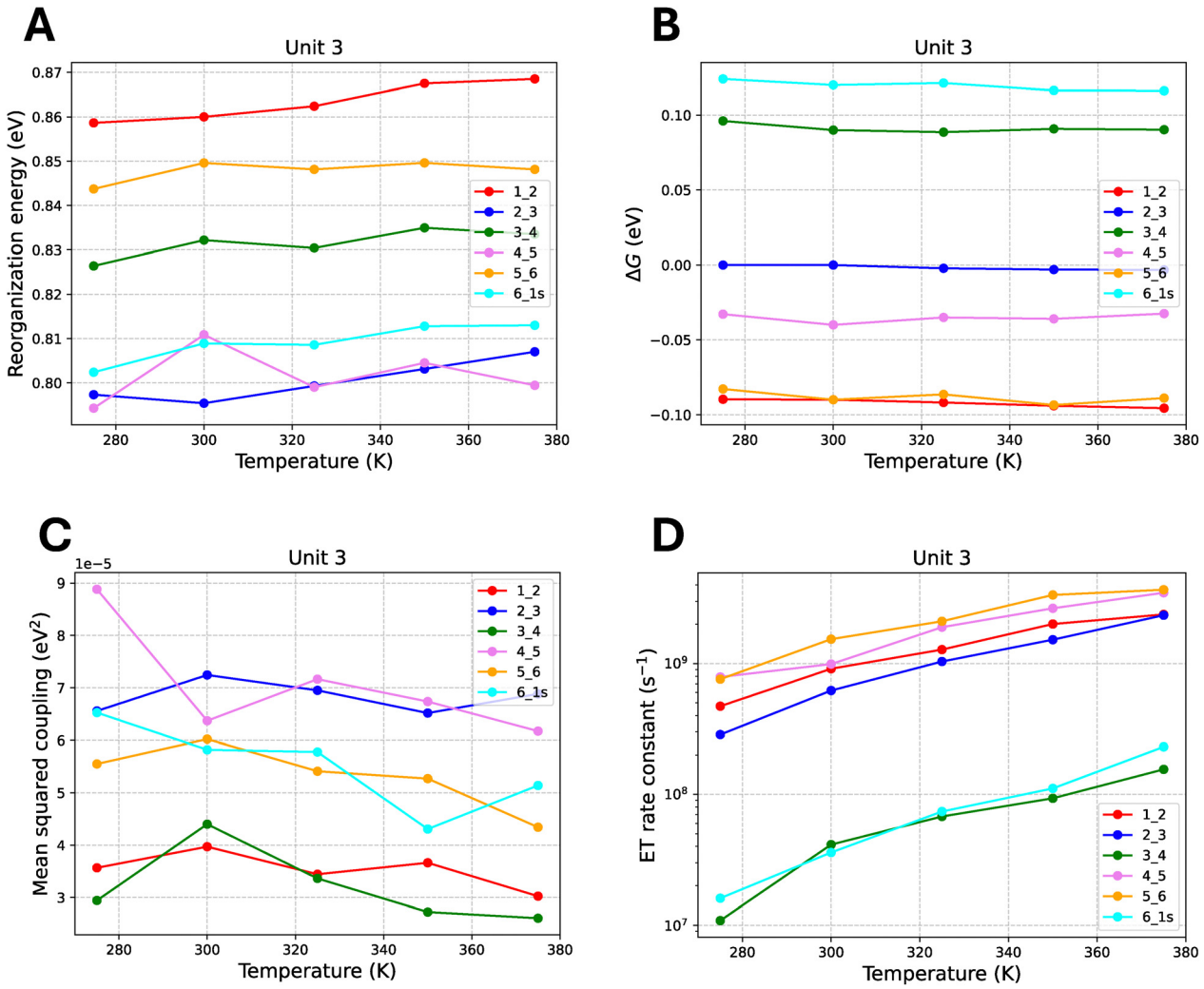

Fig. 3 Computed temperature dependent (A) reorganization energies, (B) reaction free energies, (C) mean squared electronic couplings, (D) electron transfer rate constants for *i*–*j* heme pairs in unit 3 of the OmcS heptamer.

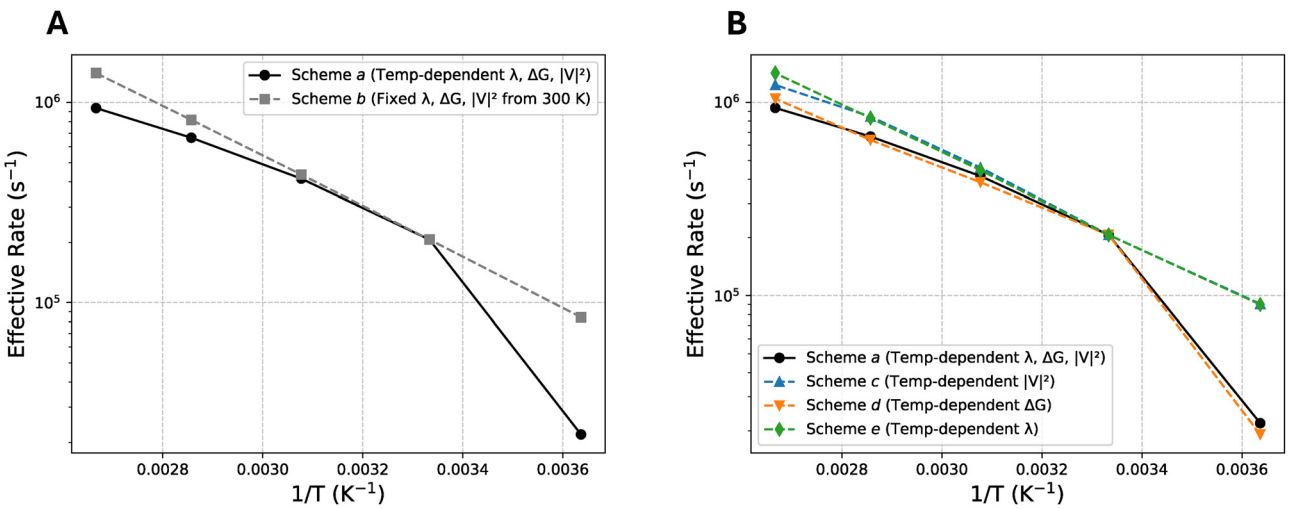

Fig. 4 Computed effective electron transport rates for different parameter schemes. (A) Comparison of scheme a (all electron transfer parameters are temperature-dependent) and scheme b (all electron transfer parameters are temperature-independent). (B) Comparison of scheme a, scheme c (only the mean-square electronic coupling is temperature-dependent), scheme d (only the reaction free energy is temperature-dependent), and scheme e (only the reorganization energy is temperature-dependent).

In scheme e, the rate increases by approximately 2.3-fold (275–300 K), 2.2-fold (300–325 K), 1.9-fold (325–350 K), and 1.7-fold (350–375 K). The rate enhancement for each temperature interval in scheme d most closely matches the rate enhancement observed in scheme a, where all electron-transfer parameters are temperature-dependent. The close agreement in the temperature-dependent rate enhancements for schemes d and a indicates that variation of the reaction free energy with temperature is the dominant factor governing the overall temperature dependence of the effective electron transport rates.

4 Conclusions

We analyzed the temperature dependence of electron-hopping transport in OmcS nanowires,[38,39] accounting for temperature-dependent protein structural changes and electrostatic effects. We used a one-dimensional transport model and the mean first passage time to assess how these temperature changes influence the transport, based on a cryo-EM structure of the OmcS heptamer.[18] As the temperature increased from 275 K to 375 K, our simulations predicted an increase in the effective electron transport rate through the nanowire. Notably, we did not predict anti-Arrhenius behavior in the simulations, in contrast to the experimental findings.[38,39]

The acceleration of the effective electron transport rates computed in our analysis does differ from the rate increase anticipated from the Arrhenius law. Arrhenius behavior predicts that the logarithm of the rate is inversely proportional to the temperature. In scheme b, where all electron transfer parameters are assumed to be temperature independent, the resulting rates follow the Arrhenius trend, with $\log(k)$ *vs.* $1/T$ slopes of −1.079 (275–300 K), −1.061 (300–325 K), −1.049 (325–350 K), and −1.040 (350–375 K), all in units of K. Our simulations from 300–375 K predict that the effective electron transport rate increases with temperature, but the rate of increase weakens as the temperature grows. In scheme a, where all electron transfer parameters are temperature-dependent, the $\log(k)$ *vs.* $1/T$ plot has slopes of −1.225, −1.057, −1.036, and −1.026 K across the same temperature intervals, respectively. Thus, between 300 K and 375 K, the computed effective electron transport rate acceleration is softer than the Arrhenius prediction. From 275 K to 300 K, the slope of the $\log(k)$ *vs.* $1/T$ plot in scheme a is −1.225, which is steeper than the Arrhenius slope of −1.079 observed in scheme b, indicating a rate enhancement that exceeds the classical Arrhenius expectation. We attribute this softened temperature dependence to the temperature dependent reaction free energies, rather than to changes in the electron transfer mechanism. We found that the temperature dependence of the reaction free energies plays the largest role in softening the rate acceleration as the temperature grows.

Our simulations find that electrostatic effects on the electron transfer parameters alone cannot account for the observed anti-Arrhenius behavior. Electrostatic effects moderate the electron-transport rate acceleration as temperature grows, but these effects are not large enough to invert the temperature dependence. The observed anti-Arrhenius transport likely arises from additional structural or dynamical changes not captured in the simulations. A missing contribution in our analysis is the influence of explicit solvent molecules on the electron transfer parameters. The implicit solvent model used here does not account for configuration-specific interactions, including hydrogen bonds between water and heme propionates, dipole–dipole interactions with nearby solvent molecules, or restructuring of the solvation shell.[92–94] Entropy effects on electron transfer rates may also be missed by the continuum model.[95,96]

A cryo-EM structure of OmcS indicates stacked hemes, with predominantly one-dimensional hopping networks under physiological conditions.[18,51,55] However, the architectures present during conductivity measurements are unknown: conductive specimens may consist of isolated filaments, bundled or cross-linked assemblies, or biofilm-embedded networks.[18,97,98] The simulations conducted here describe one-dimensional hopping transport, while alternative structures could support multidimensional pathways not captured in this model. Considerations of multidimensional transport, together with explicit solvent effects on temperature-dependent structure and electron transport, is beyond the scope of this study but may contribute to the experimental observations.

Author contributions

K. T., P. Z., and D. N. B. designed the research; K. T. performed the research; K. T., P. Z., and D. N. B. analyzed the data; and K. T., P. Z., and D. N. B. wrote the paper.

Conflicts of interest

There are no conflicts to declare.

Data availability

All data that support the findings of this study are available in the manuscript and the supplementary information (SI). The supplementary information includes: (i) an analysis of reorganization energy calculations using different dielectric constants for water-accessible cavities; (ii) computed electron transfer parameters and effective electron transport rates for units 1, 2, 4, and 5 of the OmcS heptamer; (iii) edge-to-edge distances between nearest-neighbor heme pairs and their distributions along the MD trajectories; (iv) a comparison of the computed electron transfer parameters with those reported in previous studies; and (v) protein backbone RMSD analysis of the MD trajectories. See DOI: https://doi.org/10.1039/d5cp04984a.

Acknowledgements

This material is based upon work supported by NIH grant GM-048043. K. T. acknowledges additional support from the Duke

GPNANO fellowship, Japan Student Services Organization, and the Katherine Goodman Stern Fellowship of Duke University.

References

1 W. W. Parson and A. Warshel, *J. Phys. Chem. B*, 2004, **108**, 10474–10483.
2 J. N. Gehlen, M. Marchi and D. Chandler, *Science*, 1994, **263**, 499–502.
3 N. S. Malvankar, M. Vargas, K. P. Nevin, A. E. Franks, C. Leang, B.-C. Kim, K. Inoue, T. Mester, S. F. Covalla and J. P. Johnson, *et al.*, *Nat. Nanotechnol.*, 2011, **6**, 573–579.
4 A. J. Clough, J. M. Skelton, C. A. Downes, A. A. de la Rosa, J. W. Yoo, A. Walsh, B. C. Melot and S. C. Marinescu, *J. Am. Chem. Soc.*, 2017, **139**, 10863–10867.
5 K. Lee, S. Cho, S. Heum Park, A. Heeger, C.-W. Lee and S.-H. Lee, *Nature*, 2006, **441**, 65–68.
6 O. Bubnova, Z. U. Khan, H. Wang, S. Braun, D. R. Evans, M. Fabretto, P. Hojati-Talemi, D. Dagnelund, J.-B. Arlin and Y. H. Geerts, *et al.*, *Nat. Mater.*, 2014, **13**, 190–194.
7 X. Zang, Y. Jiang, Y. Chai, F. Li, J. Ji and M. Xue, *Mater. Futures*, 2022, **1**, 011001.
8 R. H. Gilmore, S. W. Winslow, E. M. Lee, M. N. Ashner, K. G. Yager, A. P. Willard and W. A. Tisdale, *ACS Nano*, 2018, **12**, 7741–7749.
9 J. J. Hopfield, *Proc. Natl. Acad. Sci. U. S. A.*, 1974, **71**, 3640–3644.
10 R. A. Marcus and N. Sutin, *Biochim. Biophys. Acta, Bioenerg.*, 1985, **811**, 265–322.
11 N. L. Ing, R. K. Spencer, S. H. Luong, H. D. Nguyen and A. I. Hochbaum, *ACS Nano*, 2018, **12**, 2652–2661.
12 N. S. Malvankar and D. R. Lovley, *ChemSusChem*, 2012, **5**, 1039–1046.
13 N. S. Malvankar and D. R. Lovley, *Curr. Opin. Biotechnol*, 2014, **27**, 88–95.
14 R. Y. Adhikari, N. S. Malvankar, M. T. Tuominen and D. R. Lovley, *RSC Adv.*, 2016, **6**, 8354–8357.
15 S. Pirbadian, S. E. Barchinger, K. M. Leung, H. S. Byun, Y. Jangir, R. A. Bouhenni, S. B. Reed, M. F. Romine, D. A. Saffarini and L. Shi, *et al.*, *Proc. Natl. Acad. Sci. U. S. A.*, 2014, **111**, 12883–12888.
16 T. Boesen and L. P. Nielsen, *mBio*, 2013, **4**, e00270–13.
17 T. Fu, X. Liu, H. Gao, J. E. Ward, X. Liu, B. Yin, Z. Wang, Y. Zhuo, D. J. Walker and J. Joshua Yang, *et al.*, *Nat. Commun.*, 2020, **11**, 1861.
18 F. Wang, Y. Gu, J. P. O'Brien, M. Y. Sophia, S. E. Yalcin, V. Srikanth, C. Shen, D. Vu, N. L. Ing and A. I. Hochbaum, *et al.*, *Cell*, 2019, **177**, 361–369.
19 F. Wang, K. Mustafa, V. Suciu, K. Joshi, C. H. Chan, S. Choi, Z. Su, D. Si, A. I. Hochbaum and E. H. Egelman, *et al.*, *Nat. Microbiol.*, 2022, **7**, 1291–1300.
20 Y. Gu, M. J. Guberman-Pfeffer, V. Srikanth, C. Shen, F. Giska, K. Gupta, Y. Londer, F. A. Samatey, V. S. Batista and N. S. Malvankar, *Nat. Microbiol.*, 2023, **8**, 284–298.
21 Y. A. Gorby, S. Yanina, J. S. McLean, K. M. Rosso, D. Moyles, A. Dohnalkova, T. J. Beveridge, I. S. Chang, B. H. Kim and K. S. Kim, *et al.*, *Proc. Natl. Acad. Sci. U. S. A.*, 2006, **103**, 11358–11363.
22 L. Shi, D. J. Richardson, Z. Wang, S. N. Kerisit, K. M. Rosso, J. M. Zachara and J. K. Fredrickson, *Environ. Microbiol. Rep.*, 2009, **1**, 220–227.
23 L. A. Meitl, C. M. Eggleston, P. J. Colberg, N. Khare, C. L. Reardon and L. Shi, *Geochim. Cosmochim. Acta*, 2009, **73**, 5292–5307.
24 C. L. Reardon, A. Dohnalkova, P. Nachimuthu, D. W. Kennedy, D. Saffarini, B. W. Arey, L. Shi, Z. Wang, D. Moore and J. S. Mclean, *et al.*, *Geobiology*, 2010, **8**, 56–68.
25 C. Bücking, F. Popp, S. Kerzenmacher and J. Gescher, *FEMS Microbiol. Lett.*, 2010, **306**, 144–151.
26 L. Shi, K. M. Rosso, T. A. Clarke, D. J. Richardson, J. M. Zachara and J. K. Fredrickson, *Front. Microbiol.*, 2012, **3**, 50.
27 P. Subramanian, S. Pirbadian, M. Y. El-Naggar and G. J. Jensen, *Proc. Natl. Acad. Sci. U. S. A.*, 2018, **115**, E3246–E3255.
28 D. Leys, T. E. Meyer, A. S. Tsapin, K. H. Nealson, M. A. Cusanovich and J. J. Van Beeumen, *J. Biol. Chem.*, 2002, **277**, 35703–35711.
29 D. M. Shapiro, G. Mandava, S. E. Yalcin, P. Arranz-Gibert, P. J. Dahl, C. Shipps, Y. Gu, V. Srikanth, A. I. Salazar-Morales and J. P. O'Brien, *et al.*, *Nat. Commun.*, 2022, **13**, 829.
30 J. Li, E. H. Egelman and L. Craig, *J. Mol. Biol.*, 2012, **418**, 47–64.
31 H. B. Gray and J. R. Winkler, *Chem. Phys. Lett.*, 2009, **483**, 1–9.
32 J. J. Warren, M. E. Ener, A. Vlcek Jr, J. R. Winkler and H. B. Gray, *Coord. Chem. Rev.*, 2012, **256**, 2478–2487.
33 D. N. Beratan, C. Liu, A. Migliore, N. F. Polizzi, S. S. Skourtis, P. Zhang and Y. Zhang, *Acc. Chem. Res.*, 2015, **48**, 474–481.
34 D. N. Beratan, S. S. Skourtis, I. A. Balabin, A. Balaeff, S. Keinan, R. Venkatramani and D. Xiao, *Acc. Chem. Res.*, 2009, **42**, 1669–1678.
35 J. Blumberger, *Chem. Rev.*, 2015, **115**, 11191–11238.
36 D. N. Beratan, *Annu. Rev. Phys. Chem.*, 2019, **70**, 71–97.
37 C. Shih, A. K. Museth, M. Abrahamsson, A. M. Blanco-Rodriguez, A. J. Di Bilio, J. Sudhamsu, B. R. Crane, K. L. Ronayne, M. Towrie and A. Vlcek Jr, *et al.*, *Science*, 2008, **320**, 1760–1762.
38 N. L. Ing, T. D. Nusca and A. I. Hochbaum, *Phys. Chem. Chem. Phys.*, 2017, **19**, 21791–21799.
39 N. L. Ing, T. D. Nusca and A. I. Hochbaum, *Phys. Chem. Chem. Phys.*, 2018, **20**, 1294.
40 W. W. Parson, J. Huang, M. Kulke, J. V. Vermaas and D. M. Kramer, *J. Chem. Phys.*, 2024, **160**, 065101.
41 J. Bardeen and D. Pines, *Phys. Rev.*, 1955, **99**, 1140.
42 P. Klemens and R. Williams, *Int. Met. Rev.*, 1986, **31**, 197–215.
43 N. F. Polizzi, S. S. Skourtis and D. N. Beratan, *Faraday Discuss.*, 2012, **155**, 43–61.
44 M. D. Yates, J. P. Golden, J. Roy, S. M. Strycharz-Glaven, S. Tsoi, J. S. Erickson, M. Y. El-Naggar, S. C. Barton and L. M. Tender, *Phys. Chem. Chem. Phys.*, 2015, **17**, 32564–32570.

45 N. S. Malvankar, S. E. Yalcin, M. T. Tuominen and D. R. Lovley, *Nat. Nanotechnol.*, 2014, **9**, 1012–1017.
46 X. Ru, P. Zhang and D. N. Beratan, *J. Phys. Chem. B*, 2019, **123**, 5035–5047.
47 Y. Eshel, U. Peskin and N. Amdursky, *Nanotechnology*, 2020, **31**, 314002.
48 Y. Agam, R. Nandi, A. Kaushansky, U. Peskin and N. Amdursky, *Proc. Natl. Acad. Sci. U. S. A.*, 2020, **117**, 32260–32266.
49 S. Pirbadian and M. Y. El-Naggar, *Phys. Chem. Chem. Phys.*, 2012, **14**, 13802–13808.
50 S. Lampa-Pastirk, J. P. Veazey, K. A. Walsh, G. T. Feliciano, R. J. Steidl, S. H. Tessmer and G. Reguera, *Sci. Rep.*, 2016, **6**, 23517.
51 D. J. Filman, S. F. Marino, J. E. Ward, L. Yang, Z. Mester, E. Bullitt, D. R. Lovley and M. Strauss, *Commun. Biol.*, 2019, **2**, 219.
52 P. J. Dahl, S. M. Yi, Y. Gu, A. Acharya, C. Shipps, J. Neu, J. P. O'Brien, U. N. Morzan, S. Chaudhuri and M. J. Guberman-Pfeffer, *et al.*, *Sci. Adv.*, 2022, **8**, eabm7193.
53 M. J. Guberman-Pfeffer, *J. Phys. Chem. B*, 2022, **126**, 10083–10097.
54 A. Nitzan, *J. Phys. Chem. A*, 2001, **105**, 2677–2679.
55 Y. Ye, X. Liu, K. H. Nealson, C. Rensing, S. Qin and S. Zhou, *mBio*, 2022, **13**, e03822–21.
56 X. Jiang, B. Burger, F. Gajdos, C. Bortolotti, Z. Futera, M. Breuer and J. Blumberger, *Proc. Natl. Acad. Sci. U. S. A.*, 2019, **116**, 3425–3430.
57 D. A. Case, H. M. Aktulga, K. Belfon, I. Y. Ben-Shalom, J. T. Berryman, S. R. Brozell, F. S. Carvahol, D. S. Cerutti, T. E. Cheatham, G. A. Cisneros, V. W. D. Cruzeiro, T. A. Darden, N. Forouzesh, M. Ghazimirsaeed, G. Giambasu, T. Giese, M. K. Gilson, H. Gohlke, A. W. Goetz, J. Harris, Z. Huang, S. Izadi, S. A. Izmailov, K. Kasavajhala, M. C. Kaymak, I. Kolossváry, A. Kovalenko, T. Kurtzman, T. S. Lee, P. Li, Z. Li, C. Lin, J. Liu, T. Luchko, R. Luo, M. Machado, M. Manathunga, K. M. Merz, Y. Miao, O. Mikhailovskii, G. Monard, H. Nguyen, K. A. O'Hearn, A. Onufriev, F. Pan, S. Pantano, A. Rahnamoun, D. R. Roe, A. Roitberg, C. Sagui, S. Schott-Verdugo, A. Shajan, J. Shen, C. L. Simmerling, N. R. Skrynnikov, J. Smith, J. Swails, R. C. Walker, J. Wang, J. Wang, X. Wu, Y. Wu, Y. Xiong, Y. Xue, D. M. York, C. Zhao, Q. Zhu and P. A. Kollman, *Amber 2025*, University of California, San Francisco, 2025.
58 D. A. Case, H. M. Aktulga, K. Belfon, D. S. Cerutti, G. A. Cisneros, V. W. D. Cruzeiro, N. Forouzesh, T. J. Giese, A. W. Götz, H. Gohlke, S. Izadi, K. Kasavajhala, M. C. Kaymak, E. King, T. Kurtzman, T.-S. Lee, P. Li, J. Liu, T. Luchko, R. Luo, M. Manathunga, M. R. Machado, H. M. Nguyen, K. A. O'Hearn, A. V. Onufriev, F. Pan, S. Pantano, R. Qi, A. Rahnamoun, A. Risheh, S. Schott-Verdugo, A. Shajan, J. Swails, J. Wang, H. Wei, X. Wu, Y. Wu, S. Zhang, S. Zhao, Q. Zhu, T. E. Cheatham, D. R. Roe, A. Roitberg, C. Simmerling, D. M. York, M. C. Nagan and K. M. Merz, *J. Chem. Inf. Model.*, 2023, **63**, 6183–6191.
59 C. Tian, K. Kasavajhala, K. A. Belfon, L. Raguette, H. Huang, A. N. Migues, J. Bickel, Y. Wang, J. Pincay and Q. Wu, *et al.*, *J. Chem. Theory Comput.*, 2019, **16**, 528–552.
60 S. Izadi, R. Anandakrishnan and A. V. Onufriev, *J. Phys. Chem. Lett.*, 2014, **5**, 3863–3871.
61 P. Li and K. M. Merz Jr, *J. Chem. Inf. Model.*, 2016, **56**, 599–604.
62 Y. Zhang, C. Liu, A. Balaeff, S. S. Skourtis and D. N. Beratan, *Proc. Natl. Acad. Sci. U. S. A.*, 2014, **111**, 10049–10054.
63 H. B. Gray and J. R. Winkler, *Q. Rev. Biophys.*, 2003, **36**, 341–372.
64 K. A. Sharp, *Biophys. J.*, 1998, **74**, 1241–1250.
65 E. Sigfridsson, M. H. Olsson and U. Ryde, *J. Phys. Chem. B*, 2001, **105**, 5546–5552.
66 V. Tipmanee, H. Oberhofer, M. Park, K. S. Kim and J. Blumberger, *J. Am. Chem. Soc.*, 2010, **132**, 17032–17040.
67 M. K. Gilson, K. A. Sharp and B. H. Honig, *J. Comput. Chem.*, 1988, **9**, 327–335.
68 A. Nicholls and B. Honig, *J. Comput. Chem.*, 1991, **12**, 435–445.
69 L. Li, C. Li, S. Sarkar, J. Zhang, S. Witham, Z. Zhang, L. Wang, N. Smith, M. Petukh and E. Alexov, *BMC Biophys.*, 2012, **5**, 1–11.
70 C. Li, Z. Jia, A. Chakravorty, S. Pahari, Y. Peng, S. Basu, M. Koirala, S. K. Panday, M. Petukh and L. Li, *et al.*, *J. Comput. Chem.*, 2019, **40**, 2502–2508.
71 K. Siriwong, A. A. Voityuk, M. D. Newton and N. Rösch, *J. Phys. Chem. B*, 2003, **107**, 2595–2601.
72 N. Jiang, A. Kuznetsov, J. M. Nocek, B. M. Hoffman, B. R. Crane, X. Hu and D. N. Beratan, *J. Phys. Chem. B*, 2013, **117**, 9129–9141.
73 L. I. Krishtalik, *Biochim. Biophys. Acta, Bioenerg.*, 2011, **1807**, 1444–1456.
74 C. I. Bayly, P. Cieplak, W. Cornell and P. A. Kollman, *J. Phys. Chem.*, 1993, **97**, 10269–10280.
75 M. J. Frisch, G. W. Trucks, H. B. Schlegel, G. E. Scuseria, M. A. Robb, J. R. Cheeseman, G. Scalmani, V. Barone, G. A. Petersson, H. Nakatsuji, X. Li, M. Caricato, A. V. Marenich, J. Bloino, B. G. Janesko, R. Gomperts, B. Mennucci, H. P. Hratchian, J. V. Ortiz, A. F. Izmaylov, J. L. Sonnenberg, D. Williams-Young, F. Ding, F. Lipparini, F. Egidi, J. Goings, B. Peng, A. Petrone, T. Henderson, D. Ranasinghe, V. G. Zakrzewski, J. Gao, N. Rega, G. Zheng, W. Liang, M. Hada, M. Ehara, K. Toyota, R. Fukuda, J. Hasegawa, M. Ishida, T. Nakajima, Y. Honda, O. Kitao, H. Nakai, T. Vreven, K. Throssell, J. A. Montgomery, Jr., J. E. Peralta, F. Ogliaro, M. J. Bearpark, J. J. Heyd, E. N. Brothers, K. N. Kudin, V. N. Staroverov, T. A. Keith, R. Kobayashi, J. Normand, K. Raghavachari, A. P. Rendell, J. C. Burant, S. S. Iyengar, J. Tomasi, M. Cossi, J. M. Millam, M. Klene, C. Adamo, R. Cammi, J. W. Ochterski, R. L. Martin, K. Morokuma, O. Farkas, J. B. Foresman and D. J. Fox, *Gaussian 16 Revision A.03*, Gaussian Inc., Wallingford CT, 2016.
76 A. D. Becke, *J. Chem. Phys.*, 1993, **98**, 5648–5652.
77 C. Lee, W. Yang and R. G. Parr, *Phys. Rev. B: Condens. Matter Mater. Phys.*, 1988, **37**, 785.

78 F. Weigend and R. Ahlrichs, *Phys. Chem. Chem. Phys.*, 2005, **7**, 3297–3305.
79 M. Dolg, U. Wedig, H. Stoll and H. Preuss, *J. Chem. Phys.*, 1987, **86**, 866–872.
80 B. B. Owen, R. C. Miller, C. E. Milner and H. L. Cogan, *J. Phys. Chem.*, 1961, **65**, 2065–2070.
81 S. Senapati and A. Chandra, *J. Phys. Chem. B*, 2001, **105**, 5106–5109.
82 X. Jiang, J. H. van Wonderen, J. N. Butt, M. J. Edwards, T. A. Clarke and J. Blumberger, *J. Phys. Chem. Lett.*, 2020, **11**, 9421–9425.
83 C. Olea Jr, J. Kuriyan and M. A. Marletta, *J. Am. Chem. Soc.*, 2010, **132**, 12794–12795.
84 S. A. MacGowan and M. O. Senge, *Inorg. Chem.*, 2013, **52**, 1228–1237.
85 H. Santos, J. J. Moura, I. Moura, J. LeGall and A. V. Xavier, *Eur. J. Biochem.*, 1984, **141**, 283–296.
86 K. Fan, H. Akutsu, Y. Kyogoku and K. Niki, *Biochemistry*, 1990, **29**, 2257–2263.
87 B. M. Fonseca, I. H. Saraiva, C. M. Paquete, C. M. Soares, I. Pacheco, C. A. Salgueiro and R. O. Louro, *J. Biol. Inorg. Chem.*, 2009, **14**, 375–385.
88 C. A. Salgueiro, P. N. Da Costa, D. L. Turner, A. C. Messias, W. M. van Dongen, L. M. Saraiva and A. V. Xavier, *Biochemistry*, 2001, **40**, 9709–9716.
89 T. Ye, R. Kaur, X. Wen, K. L. Bren and S. J. Elliott, *Inorg. Chem.*, 2005, **44**, 8999–9006.
90 N. F. Polizzi, M. J. Therien and D. N. Beratan, *Isr. J. Chem.*, 2016, **56**, 816–824.
91 A. Bar-Haim and J. Klafter, *J. Chem. Phys.*, 1998, **109**, 5187–5193.
92 D. Laage, T. Elsaesser and J. T. Hynes, *Chem. Rev.*, 2017, **117**, 10694–10725.
93 P. Schienbein, G. Schwaab, H. Forbert, M. Havenith and D. Marx, *J. Phys. Chem. Lett.*, 2017, **8**, 2373–2380.
94 C. Soares, P. Martel, J. Mendes and M. Carrondo, *Biophys. J.*, 1998, **74**, 1708–1721.
95 P. K. Ghorai and D. V. Matyushov, *J. Phys. Chem. A*, 2006, **110**, 8857–8863.
96 D. N. LeBard and D. V. Matyushov, *J. Chem. Phys.*, 2008, **128**, 155106.
97 G. Reguera, *FEMS Microbiol. Ecol.*, 2018, **94**, fiy086.
98 S. E. Yalcin and N. S. Malvankar, *Curr. Opin. Chem. Biol.*, 2020, **59**, 193–201.